Lithos 392–393 (2021) 106138

Contents lists available at ScienceDirect

Lithos

journal homepage: www.elsevier.com/locate/lithos

Research Article

Elemental and Nd isotopic compositions of zoned titanite in mafic microgranular enclaves of the Early Cretaceous Sanguliu granitic pluton in the North China Craton: Insights into magma mixing process

Zisong Zhao [a,d], Christina Yan Wang [a,b,c,*], Bo Wei [a,b,c], Jingzhao Dou [a]

[a] CAS Key Laboratory of Mineralogy and Metallogeny, Guangzhou Institute of Geochemistry, Chinese Academy of Sciences, Guangzhou 510640, China
[b] CAS Center for Excellence in Deep Earth Science, Guangzhou 510640, China
[c] Guangdong Provincial Key Laboratory of Mineral Physics and Materials, Guangzhou 510640, China
[d] University of Chinese Academy of Sciences, Beijing 100049, China

ARTICLE INFO

Article history:
Received 2 December 2020
Received in revised form 25 March 2021
Accepted 25 March 2021
Available online 27 March 2021

Keywords:
Titanite
Zoning patterns
U–Pb dating
In situ Sm–Nd isotope
Magma mixing
North China Craton

ABSTRACT

Widespread Mesozoic granitic plutons in the North China Craton (NCC) are products of remelting of the crust associated with large-scale Mesozoic destruction of the NCC. Mafic microgranular enclaves (MMEs) are common in these plutons and are attributed to magma mixing. However, the involved magmatic processes of the mixing are poorly known. In this paper, we reported complex zoning patterns, in situ U–Pb ages, and elemental and Nd isotopic compositions of titanite grains in the MMEs and host monzogranite of the Sanguliu pluton in the NCC. Titanite grains in the MMEs and monzogranite have similar U–Pb ages of ca.130 Ma, and display different internal textures and compositions. They can thus be divided into four types, i.e., types 1 and 2 from the host monzogranite, and types 3 and 4 from the MMEs. Type 1 is euhedral in shape, whereas type 2 has a euhedral inner domain and a thin deuteric rim with a sharp contact between them. Types 3 and 4 are angular grains. Type 3 shows a typical core-mantle-rim texture with a resorbed core, a mantle and an irregular rim, whereas type 4 contains a homogeneous inner domain and a discontinuous rim. Most titanite grains of the four types display oscillatory, fir-tree and sector zoning and have crystallization temperatures ranging from 680 to 750 °C based on the Zr-in-titanite thermometry, indicating a magmatic origin. The core of type 3 titanite has the highest $\varepsilon_{Nd}(t)$ of −11.3 to −12.5 among others, close to that of the mafic dykes ($\varepsilon_{Nd}(t)$ = −7.8 to −11.6) that intrude the Sanguliu pluton. The core can be interpreted as crystallized from the mixed magmas with more mafic components that were derived from metasomatized subcontinental lithospheric mantle (SCLM) beneath the NCC. The mantle of type 3 and the inner domain of type 4 titanite have $\varepsilon_{Nd}(t)$ (−13.0 to −15.3) nearly identical to that of the MMEs (−14.3 to −15.4), but distinctly higher than that of types 1 and 2 titanite (−15.9 to −18.3). The rims of types 3 and 4 titanite have $\varepsilon_{Nd}(t)$ (−16.1 to −18.3), identical to that of type 1 and the inner domain of type 2 titanite, however, they have REE concentrations and Th/U and Nb/Ta similar to the rim of type 2 titanite, clearly indicative of crystallization from evolved, hydrated, granitic magmas. A three-stage growth model is thus proposed to explain the core-mantle-rim texture of the titanite in the MMEs by a magma mixing process. The core likely crystallized from the mixed magma with more mafic components. It was then partially or totally resorbed by mixed, dioritic magma due to chemical disequilibrium, which was followed by the re-precipitation from the dioritic magma, forming the mantle. The rim is an overgrowth from the evolved, hydrated, granitic magma. This study demonstrates that the complex zoning patterns and compositions of titanite in the MMEs can be used to investigate magmatic processes including magma mixing.

1. Introduction

Mafic microgranular enclaves (MMEs) are common in granitic plutons and are ideal to constrain the petrogenesis of granitic magmas, as well as the crust-mantle interaction (e.g., Barbarin, 2005; Vernon, 1984). The origin of the MMEs is commonly thought to be related to the mixing of mafic and felsic magmas (e.g., Barbarin, 2005; Farner

* Corresponding author at: CAS Key Laboratory of Mineralogy and Metallogeny, Guangzhou Institute of Geochemistry, Chinese Academy of Sciences, Guangzhou 510640, China.
E-mail address: wang_yan@gig.ac.cn (C.Y. Wang).

https://doi.org/10.1016/j.lithos.2021.106138
0024-4937/

et al., 2014; Plail et al., 2018; Ventura et al., 2006; Yang et al., 2007). However, the extent and consequence of magma mixing remain poorly constrained. Whole-rock chemical compositions of both the MMEs and host granitic rocks may not have information about the end-members of magmas before the mixing occurred (Flinders and Clemens, 1996; Lesher, 1990). Instead minerals, such as zircon, feldspar, apatite and titanite, in the MMEs and host granitic rocks may be used to decipher the magma mixing processes (e.g., Bruand et al., 2014; Davidson et al., 2007; Griffin et al., 2002).

Titanite ($CaTiSiO_5$) is a common accessory mineral of intermediate to felsic igneous rocks and contains a large number of elements, including Al, Fe^{2+}, Fe^{3+}, Nb, Ta, Zr, Cr, V, Mo, Mg and Sn in the Ti site, and rare earth elements (REEs), Y, Na, Mn, Pb, U, Th, Sr and Ba in the Ca site. In addition, there are OH, F and Cl in the unbonded O site (O_1) (Higgins and Ribbe, 1976; Paterson and Stephens, 1992; Frost et al., 2000; Piccoli et al., 2000). REEs and high field strength elements (HFSE, i.e., Nb, Ta, Zr, Th and U) in titanite are sensitive to the changes of temperature, pressure, oxygen fugacity (fO_2), water fugacity and melt composition (Cao et al., 2015; Mcleod et al., 2011; Nakada et al., 2016; Wones, 1989). Trace elements with low diffusion rates in titanite may record magmatic processes of the MMEs and host granitic rocks (Cherniak, 2015; Mcleod et al., 2011). Titanite can be used for U–Pb dating due to the high U (10 to 100 ppm) and high closure temperature (up to 650 to 700 °C) (Frost et al., 2000; Sun et al., 2012). Additionally, titanite has high Nd concentration and low Sm/Nd and is suitable for in situ Nd isotope analyses (Yang et al., 2008).

Voluminous Mesozoic granitic plutons in the North China Craton (NCC) were emplaced coincidently with the peak of large-scale cratonic destruction and formation of giant lode gold deposits. The Sanguliu pluton is one of these plutons and is composed of monzogranite with abundant MMEs. In this study, we identified zoned titanite grains in the MMEs and host monzogranite of the Sanguliu pluton, and presented U–Pb ages and elemental and Nd isotopic compositions of these zoned titanite grains in this paper. The new dataset enables us to investigate the magmatic processes recorded in the titanite in the MMEs. Our study may have important implications for the magma mixing processes in the generation of large-scale Mesozoic magmatism in the NCC.

2. Geological setting

The North China Craton is bounded by the central Asian orogenic belt (CAOB) to the north and the Dabie-Sulu orogenic belt to the south (Fig. 1a). The basement of the NCC is mainly composed of Paleoarchean (>3.4 Ga) metamorphic rocks (Liu et al., 1992) and supracrustal rocks and Neoarchean (2.6 to 2.5 Ga) tonalite-trondhjemite-granodiorite (TTG) suite, with minor amounts of supra-crustal rocks (2.7 to 2.5 Ga) (Wan et al., 2010; Wan et al., 2011). The basement is overlain by a thick sequence of Meso- to Neo-proterozoic and Paleozoic sedimentary rocks (Lu et al., 2008). The NCC experienced large-scale cratonic destruction in Mesozoic, which was manifested by intensive magmatism (Wu et al., 2019), formation of metamorphic core complexes (Liu et al., 2005) and pull-apart basins related to crustal extension (Davis et al., 2002), and metallogenic events (Yang and Zhou, 2002).

Voluminous Mesozoic granitic plutons occur in the northeastern part of the NCC and cover an area of over 20,000 km^2 in the Liaodong Peninsula (Lin et al., 1992). They were mainly emplaced in three periods, i.e., Triassic (233 to 210 Ma), Late Jurassic (180 to 150 Ma), and Early Cretaceous (135 to 117 Ma) (Wu et al., 2005a, 2005b; Yang et al., 2006). Triassic intrusive bodies include alkaline granite plutons in the Kuandian area and calc-alkaline granite plutons in the Xiuyan area. The late Jurassic intrusive rocks in the southern and eastern Liaodong Peninsula mainly consist of moyite, monzogranite and granodiorite, with minor plagioclase granite and quartz diorite. The Early Cretaceous igneous rocks occur extensively in the Liaodong Peninsula and comprise granite, diorite and syenite with minor gabbroic rocks.

The Sanguliu granitic pluton covers an area of about 50 km^2 in the Liaodong Peninsula. It intrudes the Jurassic gneissic granite and Proterozoic biotite granulite, sericite quartz schist, and dolomitic marble of the Liaohe Group along a NE-trending ductile shear zone (Fig. 1b). It consists of medium- to coarse-grained porphyritic moyite to monzogranite in the inner zone (Fig. 2a) and fine- to medium-grained monzogranite in the outer zone (Fig. 2b). The MMEs in the inner zone show sharp contact with the host monzogranite and most of them range in size from 10 to 20 cm (Fig. 2c, d). The MMEs in the outer zone are elliptic to irregular in shape and have transitional contact with host monzogranite. They are smaller than those in the inner zone and range in size from several centimeters to more than 10 cm (Fig. 2e, f).

3. Petrography of the Sanguliu pluton

The monzogranite of the inner zone is composed of 30–35 vol% plagioclase, 25–30 vol% K-feldspar, 20–30 vol% quartz and 10–15 vol % biotite, with minor amounts of amphibole, titanite, zircon, apatite, and allanite (Fig. 3a). The rocks show porphyritic texture; the phenocrysts are mainly composed of plagioclase and K-feldspar laths that are commonly subhedral to anhedral and range in length from 1 to 5 mm, with some being up to 15 mm, the matrix is composed of medium-grained quartz, plagioclase and biotite. The MMEs hosted in the monzogranite are composed of plagioclase (30–40 vol%), amphibole (20–30 vol%), K-feldspar (10–15 vol%), quartz (<10 vol%) and biotite (<10 vol%), minor titanite, apatite and zircon (Fig. 3b). Plagioclase and K-feldspar are subhedral to anhedral, they are fine-grained and range in length from 0.2 to 2 mm, with some being phenocrysts up to 4 mm.

The monzogranite of the outer zone contains 30–40 vol% plagioclase, 25–30 vol% K-feldspar, 25–30 vol% quartz and 10–15 vol% biotite, and minor amphibole, apatite, titanite, zircon, and allanite. Plagioclase and K-feldspar phenocrysts are subhedral to anhedral and commonly range in length from 1 to 2 mm, with some being up to 5 mm. The MMEs hosted in the monzogranite consist of 50–55 vol% plagioclase, 20–25 vol% biotite, 10–15 vol% K-feldspar, <10 vol% amphibole, <10 vol% quartz, with minor apatite, titanite and zircon. Plagioclase and K-feldspar in the MMEs range in length from 0.2 to 4 mm.

Biotite microcrystals in the MMEs of the inner zone are enclosed within amphibole (Fig. 3c), and plagioclase laths often contain dissolved cores (Fig. 3d). Acicular apatite is commonly enclosed within plagioclase (Fig. 3e). The assemblage of quartz ± plagioclase ± K-feldspar occurs in the mantle of titanite crystal and displays titanite-plagioclase ocelli texture (Fig. 3f).

4. Classification of the titanite in the MMEs and host monzogranite

As most samples in this study are collected from the inner zone of the pluton, we mainly focus on the titanite of the MMEs and host monzogranite in the inner zone. Yellowish brown titanite grains in the monzogranite are interstitial to K-feldspar, plagioclase and quartz, and rarely contain mineral inclusions (Fig. 3a). They show envelope- or diamond-like shape and range in size from 300 to 2000 μm. Oscillatory, sector and fir-tree zoning patterns are commonly observed in the BSE images of euhedral grains (Fig. 4a–d).

Titanite grains in the MMEs are interstitial to amphibole, plagioclase and quartz (Fig. 3b). They are commonly angular in shape and range in size from 200 to 1200 μm, much smaller than those in host monzogranite (Fig. 4e–i). Sector, and fir-tree zoning patterns are also observed in the cores of some grains in the MMEs (Fig. 4e, f).

The titanite in the MMEs and host monzogranite can be divided into four types on the basis of zoning patterns in the BSE images (Fig. 4).

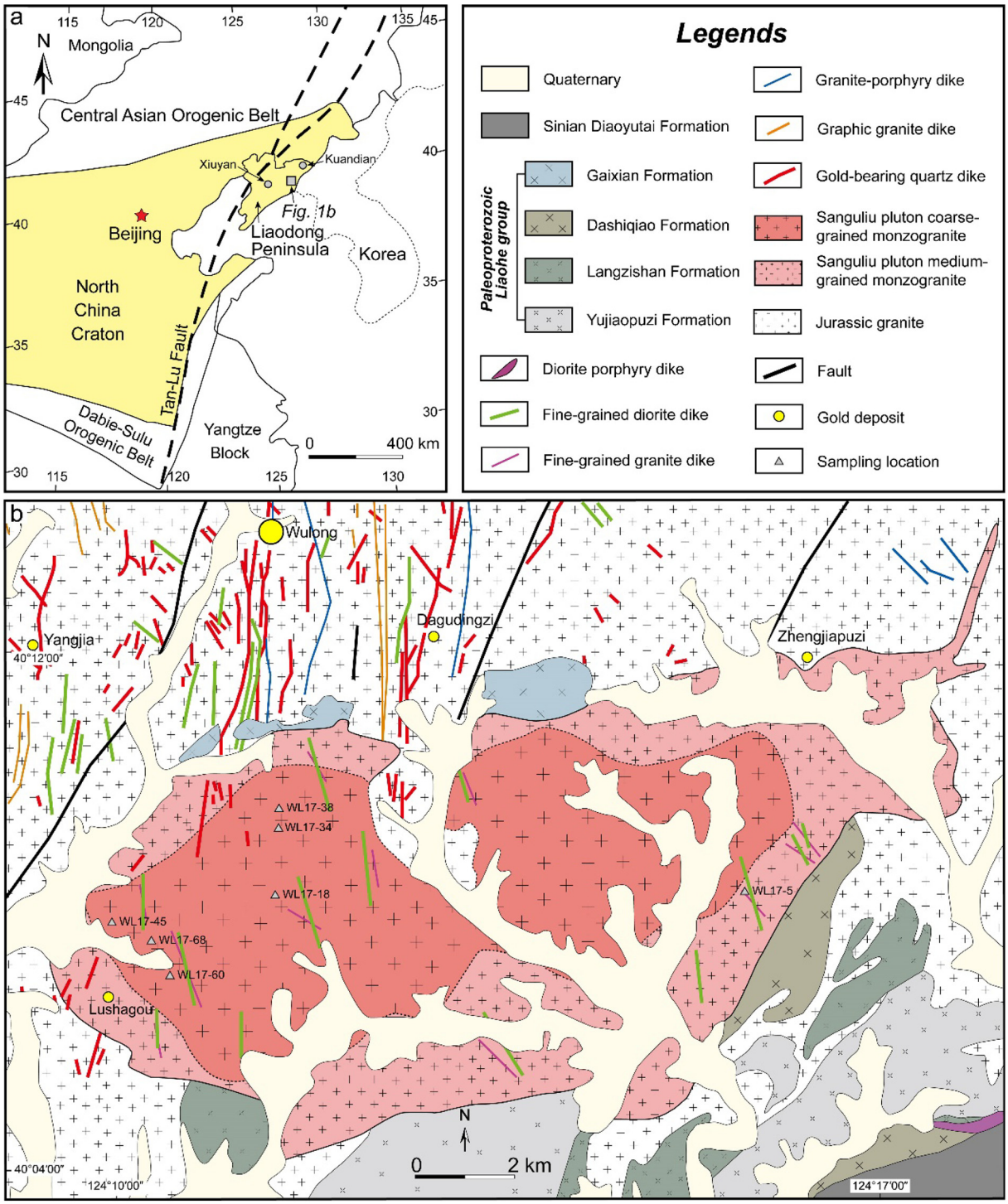

Fig. 1. (a) Simplified geological map of the North China Craton showing the location of the Sanguliu granitic pluton (modified after Wu et al., 2005a); (b) geological map of the Sanguliu granitic pluton showing the sample location and adjacent Wulong lode gold deposit.

Types 1 and 2 are mainly observed in monzogranite, whereas types 3 and 4 are mainly in the MMEs.

Type 1 titanite is typically euhedral in shape and shows distinct oscillatory, sector, and fir-tree zoning patterns (Fig. 4a–c). Type 2 titanite contains a euhedral inner domain with a thin deuteric rim, and fine-grained quartz and zircon inclusions are occasionally enclosed within the deuteric rim (Fig. 4d). The deuteric veinlets penetrate the inner domain in local places (close-up in Fig. 4d). Overall, type 1 is more common than type 2 in the monzogranite.

Type 3 titanite is anhedral with typical core-mantle-rim texture (Fig. 4e, f). The core develops sector and fir-tree zoning; however, it is irregular in shape and shows embayment outline, the mantle is characterized by the presence of abundant quartz, amphibole and plagioclase inclusions, and the rim is typically corroded. Type 4 titanite is angular,

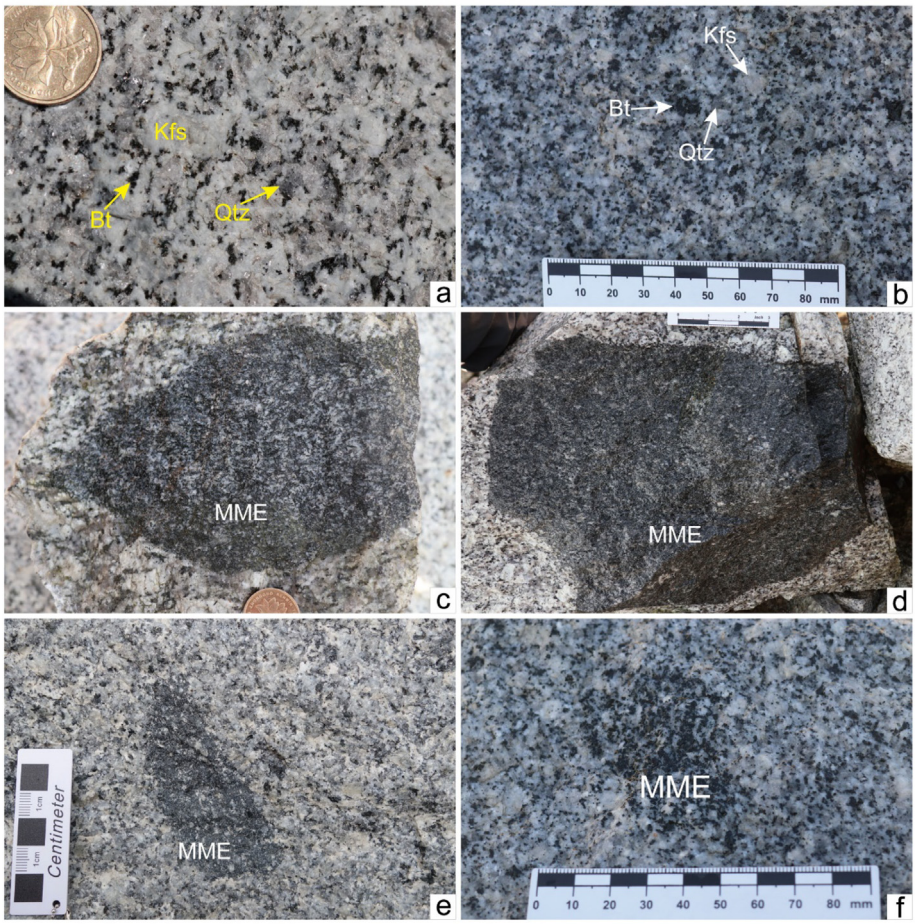

Fig. 2. Field photos of monzogranite and mafic microgranular enclaves (MMEs) of the Sanguliu granitic pluton. (a) and (b) Monzogranite in the inner zone and outer zone of the pluton; (c) and (d) the MMEs in the inner zone of the pluton; (e) and (f) the MMEs in the outer zone of the pluton.

containing an inner domain similar to the mantle of type 3 titanite, and a rim similar to the rim of type 3 titanite (Fig. 4g–i). Overall, type 4 is more common than type 3 in the MMEs.

5. Analytical methods

5.1. Major element analyses of minerals

Major elements of titanite and amphibole were analyzed using a JEOL JXA-8230 electron probe microanalyzer (EPMA) at the CAS Key Laboratory of Mineralogy and Metallogeny. The operating conditions were at 15 kV and 20 nA with a beam spot size of ~1 μm. The peak and background counting times were 40s and 20s for Ti, Mn and Mg, 20s and 10s for Si, Fe, Ca and Al, and 10s and 5 s for F, Cl, K and Na, respectively. American SPI standard materials: rutile (Ti), olivine (Si), olivine (Mg), Cr-diopside (Ca), magnetite (Fe), almandine (Al), rhodonite (Mn), orthoclase (K), albite (Na), BaF_2 (F) and tugtupite (Cl) were used as standards. All data were processed with ZAF correction and element detection limit is 0.01%.

5.2. U–Pb dating, trace element and Sm–Nd isotope analyses for titanite

The U–Pb age and trace elements of titanite were analyzed in situ by an Agilent 7500a Q-ICPMS equipped with a GeoLas Pro-type 193 nm excimer laser ablation system at Institute of Geology and Geophysics, Chinese Academy of Sciences (IGGCAS). A beam spot size of 32 μm was employed to analyze under 6 Hz ablation repetition rate. Detailed analytical technique is given in Sun et al. (2012). The measured composition of titanite was plotted on the Tera-Wasserburg diagram (Tera and Wasserburg, 1972) and defined a line intersecting the y-axis at common $^{207}Pb/^{206}Pb$ composition. The lower intercepts approximately represent of formation ages of the samples. The measured ^{207}Pb composition was used for common Pb correction. The Tera-Wasserburg diagram and weighted mean $^{206}Pb/^{238}U$ age were calculated using Isoplot (v4.15) (Ludwig, 2012). BLR-1(1047.1 ± 0.4 Ma, Ma et al., 2019) and Ontario (1053.3 ± 3.1 Ma, Ma et al., 2019) are used as the external and monitor standard of the U–Pb dating. The obtained $^{206}Pb/^{238}U$ age of BLR-1 and Ontario in our analyses is 1044.9 ± 14 Ma and 1049.0 ± 12 Ma, respectively, which are consistent with aforementioned reference values within uncertainty (Supplementary Table S1).

Trace element contents of titanite are calibrated against ^{43}Ca as the internal standard and NIST 610 as the external standard (CaO content in titanite refers to the average composition measured by EPMA). The recommended trace element contents of NIST 610 are compared with the obtained values of this study (Supplementary Table S2). The raw data were processed by GLITTER 4.0 software (GEMOC, Macquarie University) (Griffin, 2008).

The Sm–Nd isotopic composition of titanite was measured in situ for the grains that have U–Pb ages, using a Neptune multi-collector (MC)-ICPMS equipped with a GeoLas-type 193 nm excimer laser ablation system at IGGCAS. A single-point analysis mode was used with a beam spot diameter of 44 μm under ablation frequency of 6 Hz and laser fluence of ~6 J/cm^2. BLR-1 and Ontario are used as the standards during analyses. The $^{147}Sm/^{144}Nd$ and $^{143}Nd/^{144}Nd$ were calibrated using exponential law after correcting for the isobaric interference of ^{144}Sm on ^{144}Nd.

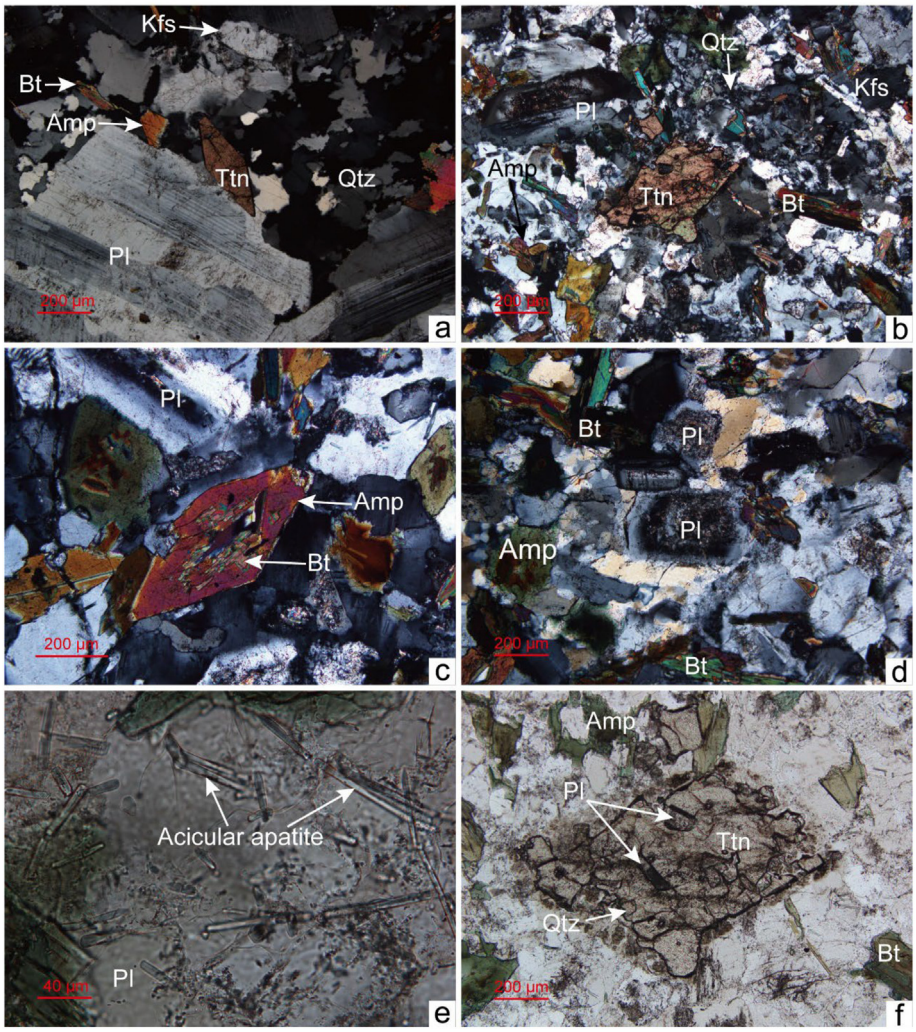

Fig. 3. Microphotographs of monzogranite and mafic microgranular enclaves (MMEs) of the Sanguliu granitic pluton. (a) Medium- to coarse-grained biotite monzogranite shows porphyritic texture with plagioclase (Pl) phenocrysts, biotite (Bt), amphibole (Amp), K-feldspar (Kfs), and titanite (Ttn) is interstitial to plagioclase and quartz (Qtz). Under cross-polarized and transmitted light, sample WL17–34; (b) the MME is mainly composed of plagioclase and amphibole, and titanite is interstitial to biotite, K-feldspar and quartz. Under cross-polarized and transmitted light, sample WL17–60; (c) biotite microcrystal in the MME is enclosed within amphibole, showing a disequilibrium texture. Under cross-polarized and transmitted light, sample WL17–60; (d) the core of plagioclase lath in the MME is dissolved due to chemical disequilibrium. Under cross-polarized and transmitted light, sample WL17–60; (e) acicular apatite (Ap) within the plagioclase of the MME, showing a quenched texture. Under plane-polarized and transmitted light, sample WL17–60; (f) titanite-plagioclase ocelli developed in the mantle of the titanite in the MME with a zone of quartz ± plagioclase ± K-feldspar. Under plane-polarized and transmitted light, sample WL17–60.

Detailed instrument and measurement conditions are given in Yang et al. (2008), Wu et al. (2010), and Ma et al. (2019). BLR-1 was reported to have $^{147}Sm/^{144}Nd$ of ~0.1939 (45) and $^{143}Nd/^{144}Nd$ of ~0.512829 (47), and Ontario was reported to have $^{147}Sm/^{144}Nd$ of ~0.1916 (32) and $^{143}Nd/^{144}Nd$ of ~0.512815 (41) (Ma et al., 2019). In this study, BLR-1 was measured to have $^{147}Sm/^{144}Nd$ of 0.1937 (2) and $^{143}Nd/^{144}Nd$ of 0.512832 (70), and Ontario to have $^{147}Sm/^{144}Nd$ of 0.1938 (2) and $^{143}Nd/^{144}Nd$ of 0.512837 (80), which are consistent with aforementioned reference values within uncertainties (Supplementary Table S3).

5.3. Trace element mapping for titanite

Trace element mapping of titanite was performed in the Mineral Microanalysis Laboratory of the Ore Deposit and exploration Centre (ODEC) of the School of Resources and Environmental Engineering, Hefei University of Technology. A laser ablation system is made up of Agilent 7900 ICP-MS equipped with a 193-nm ArF excimer laser (PhotonMachines Analyte HE). The sample was measured with a beam size of 15–40 μm while sample was moving with a speed of 15–40 μm/s under 10 Hz repetition rate and laser ablation energy of 2–3 J/cm^2. About 20s of background signal was collected during pre- and post-analyzing. GSD-1G was adopted as the external standard. The final trace element mapping images were calibrated based on the probability density distribution function. Data analyses and mapping were performed using Geochemistry-SoftWareV4. More details refer to Wang et al. (2017).

6. Results

6.1. Titanite U–Pb ages

Titanite grains from two monzogranite samples (WL17–18 and WL17–38) were analyzed for U–Pb ages (Supplementary Table S1). The upper intercepts of the data for the two samples correspond to $^{207}Pb/^{206}Pb$ of 0.84 ± 0.04 and 0.84 ± 0.02, respectively, in the Tera-Wasserburg U–Pb plots (Fig. 5a, b). The obtained lower intercept age is 130.3 ± 1.8 Ma (MSWD = 1.5) for sample WL17–18 (Fig. 5a) and 130.5 ± 2.5 Ma (MSWD = 2.5) for sample WL17–38 (Fig. 5b), consistent with the weighted mean $^{206}Pb/^{238}U$ age of 129.9 ± 1.7 Ma

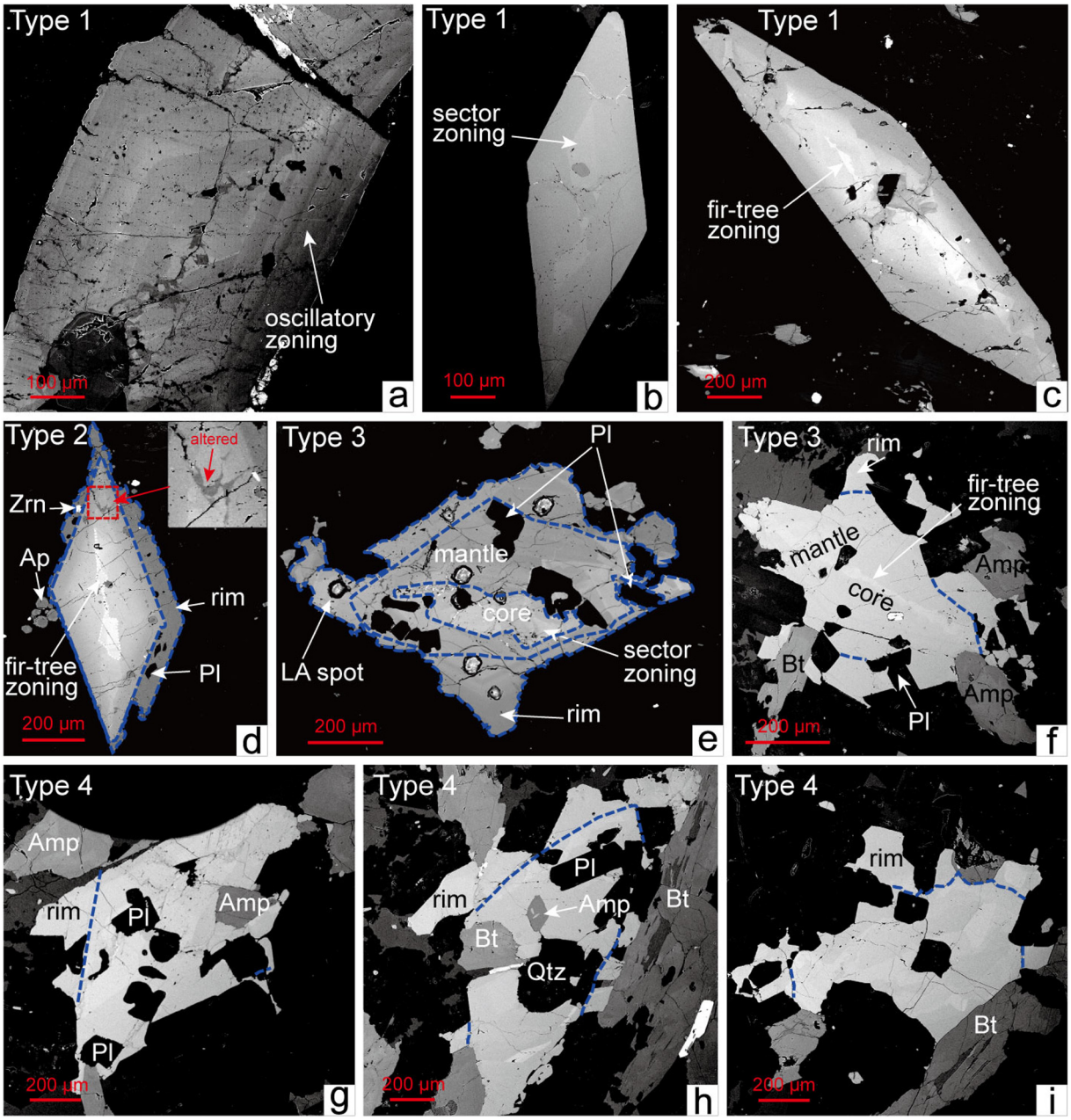

Fig. 4. BSE images of the four types of titanite in the monzogranite and mafic microgranular enclaves (MMEs) of the Sanguliu granitic pluton. (a)-(c) Type 1 titanite in monzogranite showing oscillatory zoning, sector zoning and fir-tree zoning; (d) type 2 titanite in monzogranite showing fir-tree zoning and a thin deuteric rim, zircon (Zrn) inclusions are enclosed in the rim; (e)-(f) type 3 titanite in the MMEs showing the core-mantle-rim texture, with sector and fir-tree zoning in the core; (g)-(i) type 4 titanite in the MMEs contains an inner domain and rim.

(MSWD = 1.0; $n = 23$) and 130.5 ± 1.9 Ma (MSWD = 1.5; $n = 29$) for the two samples (inset in Fig. 5a, b).

Titanite grains from three MMEs samples (WL17–5, WL17–45, and WL17–60) were analyzed for U–Pb ages (Supplementary Table S1). The upper intercepts of the data for the three samples correspond to $^{207}Pb/^{206}Pb$ of 0.84 ± 0.02, 0.84 ± 0.04, and 0.84 ± 0.01, respectively, in the Tera-Wasserburg U–Pb plots (Fig. 5c–e). The data yielded the lower intercept age of 129.6 ± 1.3 Ma (MSWD = 0.91) for sample WL17–5 (Fig. 5c), 129.9 ± 1.9 Ma (MSWD = 2.5) for sample WL17–45 (Fig. 5d), and 130.5 ± 2.2 Ma (MSWD = 0.68) for sample WL17–60 (Fig. 5e). These ages are identical to the weighted mean $^{206}Pb/^{238}U$ age of 129.4 ± 1.4 Ma (MSWD = 0.68; $n = 35$), 129.7 ± 2 Ma (MSWD = 0.58; $n = 25$), and 129.5 ± 2.1 Ma (MSWD = 0.54; $n = 31$) within analytical error for the three samples (inset in Fig. 5c–e).

The results indicate that the titanite in the MMEs have nearly identical crystallization age to that of the titanite in host monzogranite. The obtained U–Pb ages of the titanite in this study are also similar to the zircon U–Pb ages reported for the Sanguliu pluton in the literature (Wei et al., 2003; Wu et al., 2005a).

6.2. Major and trace element compositions of titanite

The titanite grains of the MMEs and host monzogranite overall have negative correlation of Al + Fe (apfu) and Ti (apfu) except for a few outliers that were analyzed for the rims of types 2 and 3 titanite (Fig. 6a and Supplementary Table S2). They also show negative correlation of F (apfu) and Ti (apfu) and Ca (apfu) and REE + Y (Fig. 6b, c). The rim

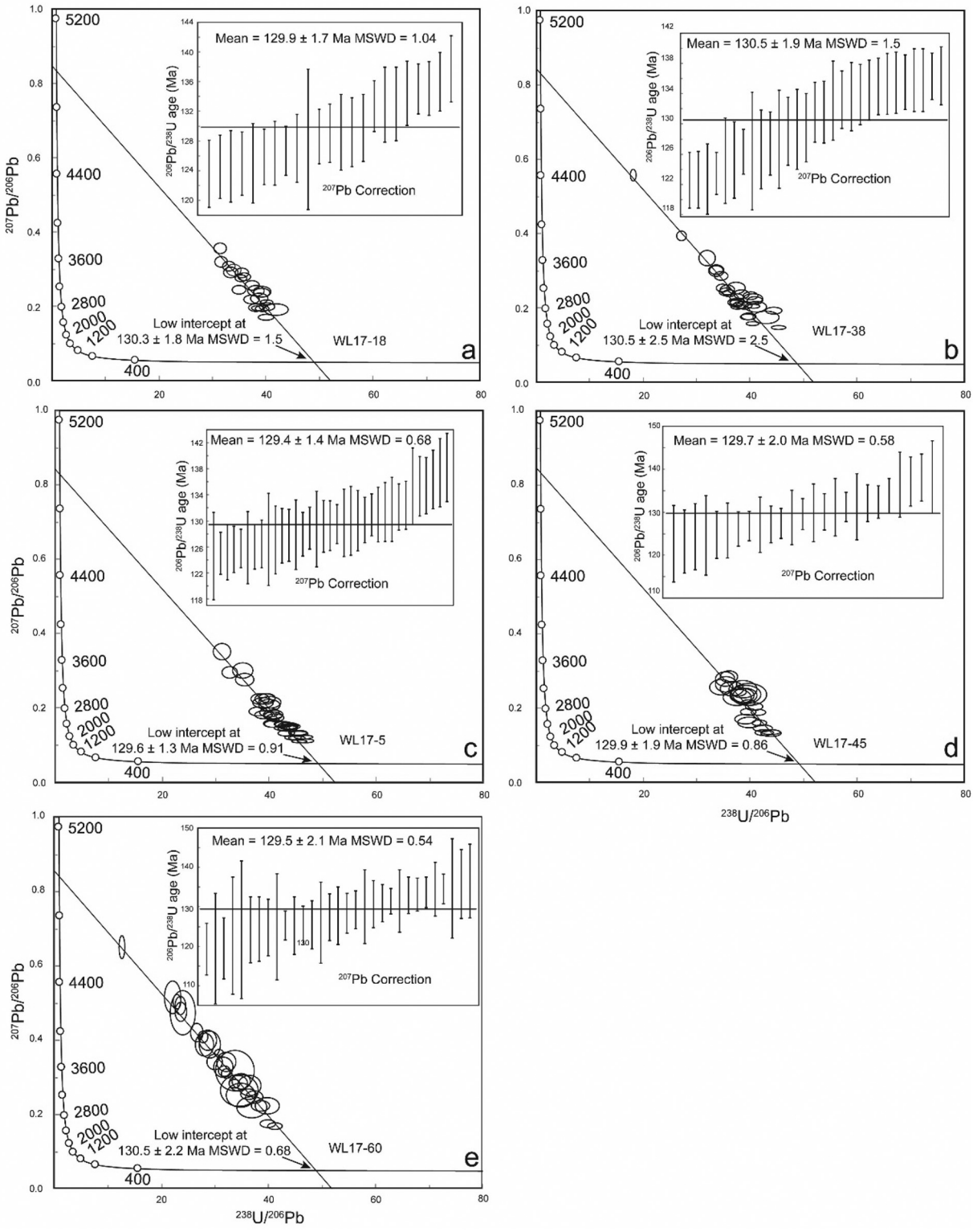

Fig. 5. Tera–Wasserburg U–Pb plots for the titanite in the monzogranite and mafic microgranular enclaves (MMEs) of the Sanguliu granitic pluton. (a)-(b) Titanite of sample WL17–18 and WL17–38 from monzogranite in the inner zone of the pluton; (c)-(e) titanite of sample WL17–45 and WL17–60 from the MMEs in the inner zone, and titanite of sample WL17–5 from the MMEs in the outer zone of the pluton.

overall has high F and Ca and low REE + Y relative to those for the core, mantle and inner domain of the titanite (Fig. 6b, c).

Type 1 titanite and the core, mantle and inner domain of types 2, 3 and 4 titanite have similar REE concentrations and patterns with very negative Eu anomalies on the chondrite-normalized REE patterns (Fig. 7a–d). The mantle of type 3 titanite has flat HREE pattern, contrast to right-sloped HREE pattern for the core (Fig. 7c).

The rim of type 2 titanite has REE lower than the inner domain and shows positive Eu anomaly ($\delta Eu = 0.72$ to 1.95) on the REE patterns (Fig. 7b). The rims of types 3 and 4 titanite have much lower REE

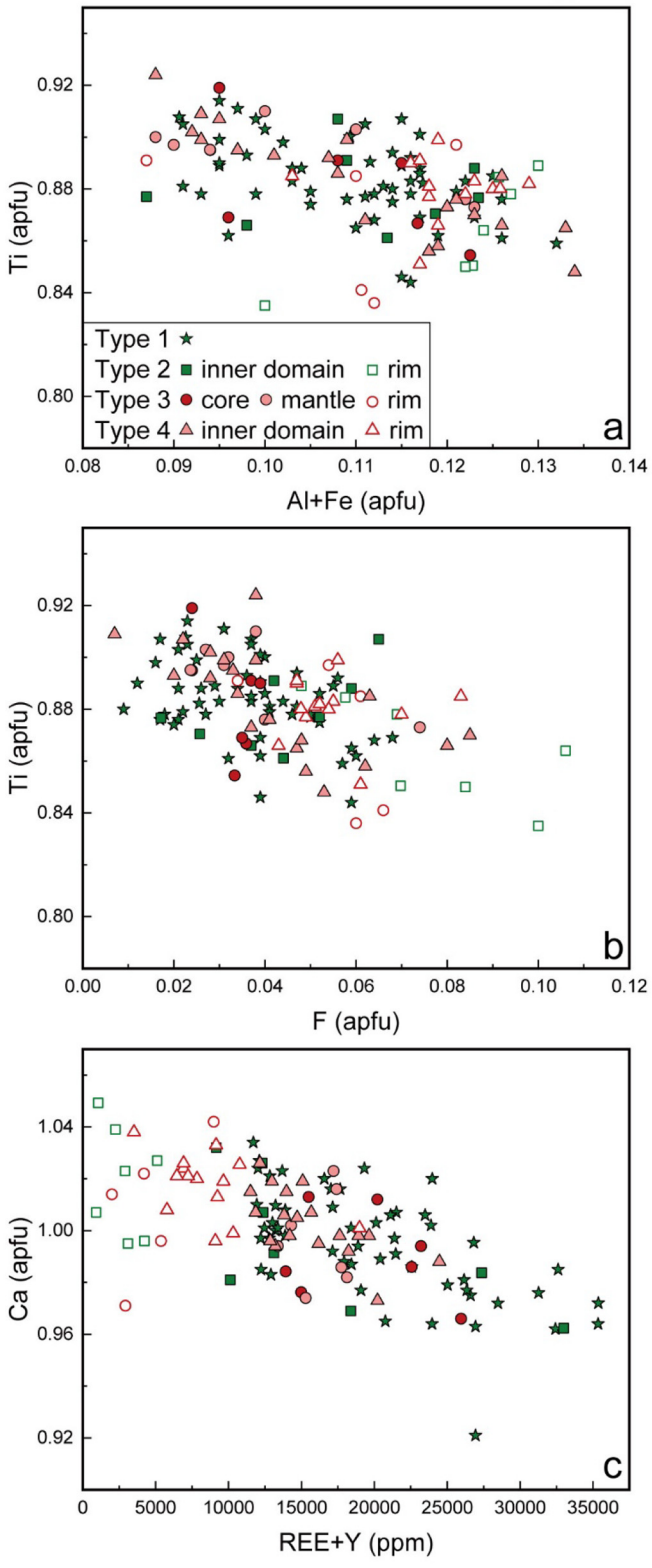

Fig. 6. Plots of (Fe + Al) versus Ti (a), F versus Ti (b), and (REE + Y) versus Ca (c) for the four types of titanite in the MMEs and host monzogranite of the Sanguliu granitic pluton.

concentrations than their respective mantle and inner domain, but they have similar REE patterns (Fig. 7c, d).

Type 1 titanite and the core, mantle and inner domain of types 2, 3 and 4 titanite contain Nb and Ta higher than the rims of types 2, 3 and 4 titanite (Fig. 8a). Type 1 titanite and the core, mantle and inner domain of types 2, 3 and 4 titanite have highly variable Th/U and restricted low Nb/Ta and δEu, remarkably different from restricted low Th/U and highly variable Nb/Ta and δEu of the rims of types 2, 3 and 4 titanite (Fig. 8b, c). In addition, either rim or core, mantle and inner domain of the titanite have similarly highly variable La/Yb, Zr/Hf and δCe (Fig. 8d-f).

6.3. Sm–Nd isotopic compositions of titanite

Type 1 titanite and the inner domain of type 2 titanite overall have $\varepsilon_{Nd}(t = 130\ Ma)$ values ranging from −15.9 to −18.3 (Supplementary Table S3). However, it is noted that a single crystal of type 1 and the inner domain of type 2 titanite usually has similar $\varepsilon_{Nd}(t)$ values in different parts (e.g., Fig. 9a).

The core of type 3 titanite has the highest $\varepsilon_{Nd}(t)$ (−11.3 to −12.5) among all four types of the titanite (Fig. 9d and Supplementary Table S3). The mantle of type 3 and the inner domain of type 4 titanite have $\varepsilon_{Nd}(t)$ ranging from −13.0 to −15.3, slightly lower than that of the core of type 3 titanite (Fig. 9d and Supplementary Table S3). The rims of types 3 and 4 titanite have $\varepsilon_{Nd}(t)$ ranging from −16.1 to −18.3, nearly identical to those of type 1 and the inner domain of type 2 titanite (Fig. 9d and Supplementary Table S3).

Type 1 and the inner domain of type 2 titanite exhibit nearly positive correlation of $^{147}Sm/^{144}Nd$ and $^{143}Nd/^{144}Nd$ (Fig. 9c). The core of type 3 titanite has the highest $^{143}Nd/^{144}Nd$ among others, whereas the mantle of type 3 titanite have similar $^{143}Nd/^{144}Nd$ to that of the inner domain of type 4 titanite. They both have $^{143}Nd/^{144}Nd$ higher than that for the rims of types 3 and 4, and type 1 and the inner domain of type 2 titanite (Fig. 9c). In contrast, the rims of types 3 and 4 titanite have similar ranges of $^{143}Nd/^{144}Nd$ and $^{147}Sm/^{144}Nd$ to that of type 1 and the inner domain of type 2 titanite (Fig. 9c). On the plot of $\varepsilon_{Nd}(t)$ versus Nb/Ta, the rims of types 3 and 4 titanite have Nb/Ta negatively correlated with $\varepsilon_{Nd}(t)$, whereas others show highly variable $\varepsilon_{Nd}(t)$ against relatively restricted Nb/Ta (Fig. 9d).

7. Discussion

The sector, fir-tree and oscillatory zoning patterns are commonly observed in type 1 and the inner domain and core of types 2, 3 and 4 titanite (Fig. 4). The crystallization temperatures for the core, mantle and inner domain of the titanite are estimated to be 683 to 749 °C using the Zr-in-titanite geothermometer (Hayden et al., 2008), in which a_{TiO_2} is assumed to be 0.5 and a_{SiO_2} is assumed to be 1. The high crystallization temperature of the titanite indicates a magmatic origin (*c.f.*, Paterson and Stephens, 1992; Watson and Liang, 1995; Mcleod et al., 2011; Olierook et al., 2019). On the other hand, the crystallization temperature of the rim of type 2 titanite is estimated to be 613 to 658 °C (Fig. 10), lower than the water-saturated solidus of granite (680 °C, Johannes and Holtz, 1996), indicating that the rim may have developed under subsolidus condition. The rims of types 3 and 4, however, have crystallization temperatures (623 to 684 °C) slightly higher than that of the rim of type 2 (Fig. 10). In contrast to relatively homogeneous, euhedral types 1 and 2 in host monzogranite, the diverse core-mantle-rim textures and chemical compositions of types 3 and 4 titanite in the MMEs of the Sanguliu pluton may have insights for complex growth processes during magma mixing.

7.1. Origin of the titanite in host monzogranite

Type 1 titanite and the inner domain of type 2 have Nb/Ta ranging from 4.7 to 16.6, similar to that for the titanite of the Early Cretaceous Guojialing and Fanshan granitic plutons in the NCC (Fig. 8b), but much lower than that of metamorphic or hydrothermal titanite (Nb/Ta>20; Chen et al., 2013; Chen and Zheng, 2015; Fu et al., 2016). They have $\varepsilon_{Nd}(t)$ values ranging from −15.9 to −18.3, overlapping with that of host monzogranite ($\varepsilon_{Nd}(t)$ = −18.3 to −20.1) (Fig. 9e), indicating

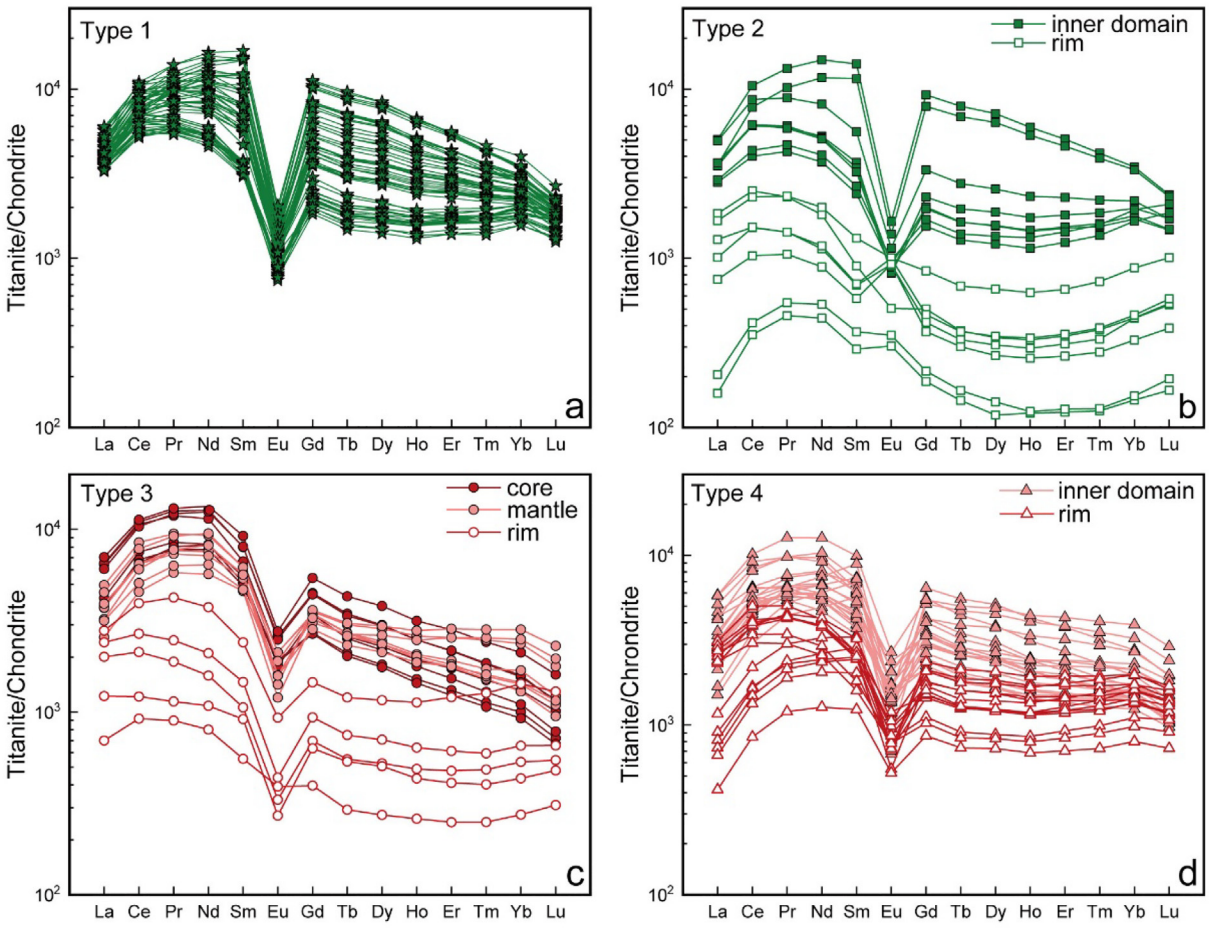

Fig. 7. Chondrite-normalized rare earth element patterns for the four types of titanite in the MMEs and host monzogranite of the Sanguliu granitic pluton. Chondrite normalization values are from Sun and McDonough (1989).

that type 1 and the inner domain of type 2 titanite may have been in Nd isotope equilibrium with granitic magmas during crystallization.

When titanite crystallizes from granitic magmas, Fe^{3+} tends to substitute Ti^{4+} in the octahedral site of the titanite lattice at high temperatures due to their similar ionic radius (Shannon, 1976), whereas the REE commonly substitute Ca^{2+} (Green and Pearson, 1986). The substitution reactions can be shown as $Ca^{2+} + Ti^{4+} \Leftrightarrow (REE, Y)^{3+} + (Fe, Al)^{3+}$ (Green and Pearson, 1986). These reactions can cause the negative correlation of Ti versus Al + Fe and REE + Y versus Ca of the titanite (Fig. 6a, c), respectively. The REE zoning of type 2 titanite (Fig. 11) can be also attributed to the substitution of Ca^{2+} by REE^{3+} and Y^{3+} (Olierook et al., 2019). The negative Eu anomaly of type 1 and the inner domain of type 2 titanite (Fig. 7a, b) likely results from fractionation of plagioclase, indicating that the titanite crystallized later than plagioclase in the monzogranite. Therefore, type 1 and the inner domain of type 2 titanite are likely attributed to crystallization from granitic magmas of the Sanguliu pluton.

7.2. Origin of the titanite in the MMEs

The titanite in the MMEs and host monzogranite yielded similar U–Pb ages (Fig. 5), indicating that the MMEs and monzogranite may have crystallized simultaneously in the magma chamber. The MMEs show typical igneous texture (Fig. 3b), so they are not either xenolith or restite. The MMEs have Sr–Nd isotopic compositions distinctly different from that of host monzogranite of the Sanguliu pluton (Fig. 9e), ruling out that the MMEs were early crystalline phases of granitic magmas. The disequilibrium textures in the MMEs (Fig. 3c, d) are ascribed to the change of temperature and melt compositions and are direct evidence for magma mixing (*c.f.*, Baxter and Feely, 2002; Jiang et al., 2016; Hibbard, 1981). The mixed magmas may have been injected into the granitic magma chamber and crystallized under high degrees of undercooling, leaving a sharp contact between the MMEs and host monzogranite. They may have crystallized rapidly at the emplacement level so that some quenched textures were also developed in the MMEs. Acicular apatite in plagioclase (Fig. 3e) and fine-grained texture of the MMEs (Fig. 3b) are consistent with fast cooling of the MMEs (*c.f.*, Baxter and Feely, 2002).

The mantle of type 3 titanite has $\varepsilon_{Nd}(t)$ (−14.3 to −15.3) similar to that of the MMEs (−14.3 to −15.9), so it may have crystallized from the mixed magmas. However, the core of type 3 titanite has $\varepsilon_{Nd}(t)$ (−11.3 to −12.5) close to that of the mafic dyke ($\varepsilon_{Nd}(t) = -7.8$ to −11.6) that intrudes the Sanguliu pluton (Fig. 9e). It is noted that the maximum $\varepsilon_{Nd}(t)$ value of the mafic dyke is similar to that of the subcontinental lithospheric mantle (SCLM) beneath the NCC ($\varepsilon_{Nd}(t) = -6.0$ on average, Yang et al., 2004), whereas the host monzogranite has $\varepsilon_{Nd}(t)$ close to that of ancient lower crust of the NCC ($\varepsilon_{Nd}(t) = -22.5$ on average, Yang et al., 2004) (Fig. 9e). The degree of magma mixing can be thus estimated by assuming that the MMEs are mixing products of a mantle-derived mafic magma and a crustal-derived felsic magma. For the mafic end-member, we used the SCLM beneath the NCC (Yang et al., 2004). For the felsic end-member, we used the ancient lower crust of the NCC (Yang et al., 2004). Using the Sr–Nd isotopic compositions of these two end-members gives a good fit for the data of the titanite and MMEs in this study (Fig. 9e). The results indicate that the MMEs may have crystallized from the mixed magmas composed of

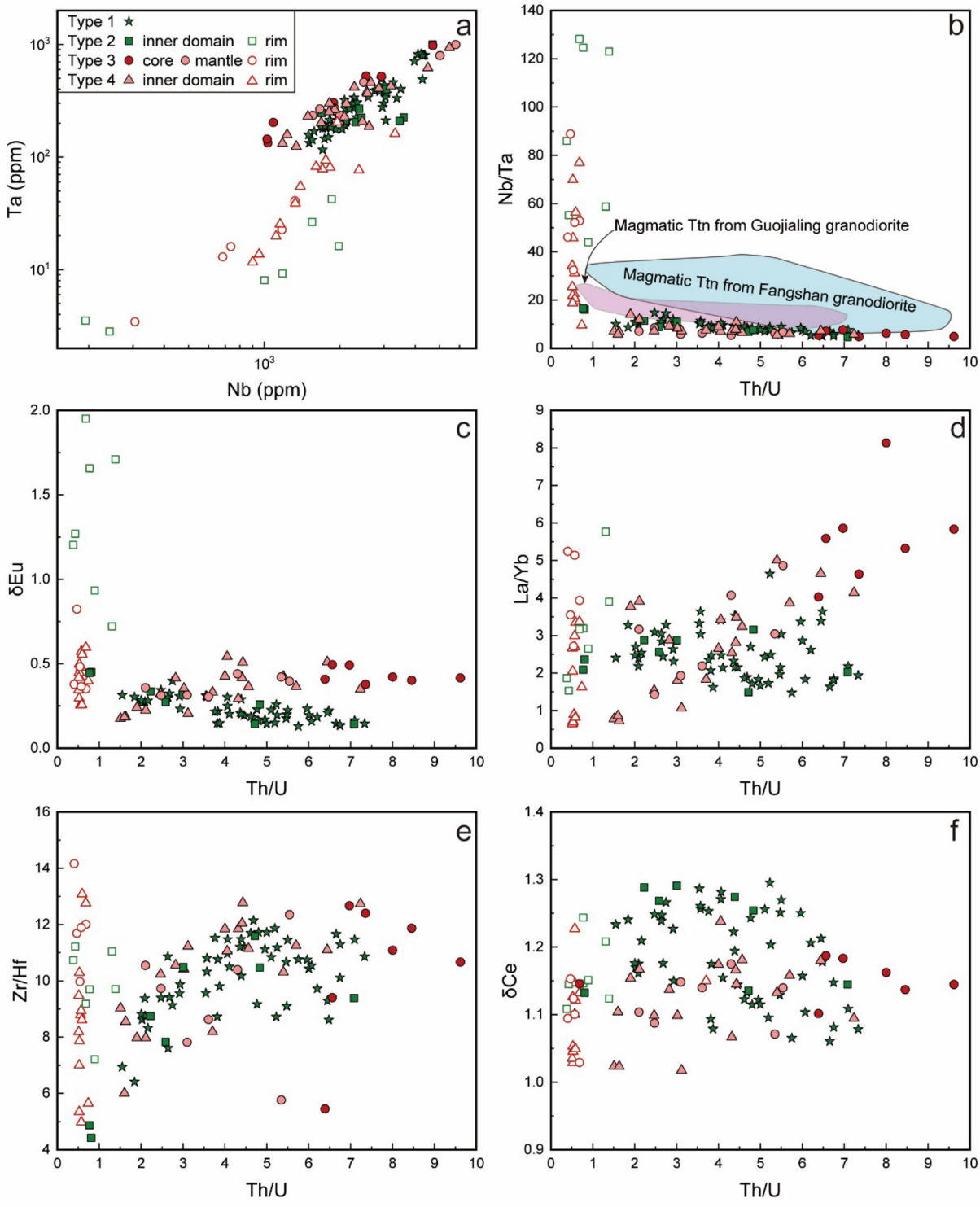

Fig. 8. Plots of Nb versus Ta (a), and Th/U versus Nb/Ta (b), δEu (c), La/Yb (d), Zr/Hf (e), δCe (f) for the four types of titanite in the MMEs and host monzogranite of the Sanguliu granitic pluton. Data source: Guojialing granodiorite (Jiang et al., 2016); Fangshan granodiorite (Sun et al., 2010).

~30% mafic component and ~ 70% felsic component (Fig. 9e). However, the mixed magmas were likely heterogeneous spatially and temporally, so that the core and mantle of type 3 titanite may have crystallized from different stages during magma mixing. The core of type 3 titanite likely crystallized earlier from the mixed magmas with a greater fraction of mafic components (i.e., 45 to 55%) (Fig. 9e). This is consistent with the observation that the core of type 3 titanite has La/Yb higher than those of type 1 titanite (Fig. 8d), because the partition coefficient ratios of LREE/HREE for the titanite crystallized from mafic magmas are remarkably higher than those for the titanite crystallized from granitic magmas (Prowatke and Klemme, 2005).

7.3. Origin of titanite rims

The rims of types 3 and 4 titanite have $\varepsilon_{Nd}(t)$ from −16.6 to −18.3, nearly identical to that of type 1 titanite and inner domain of type 2

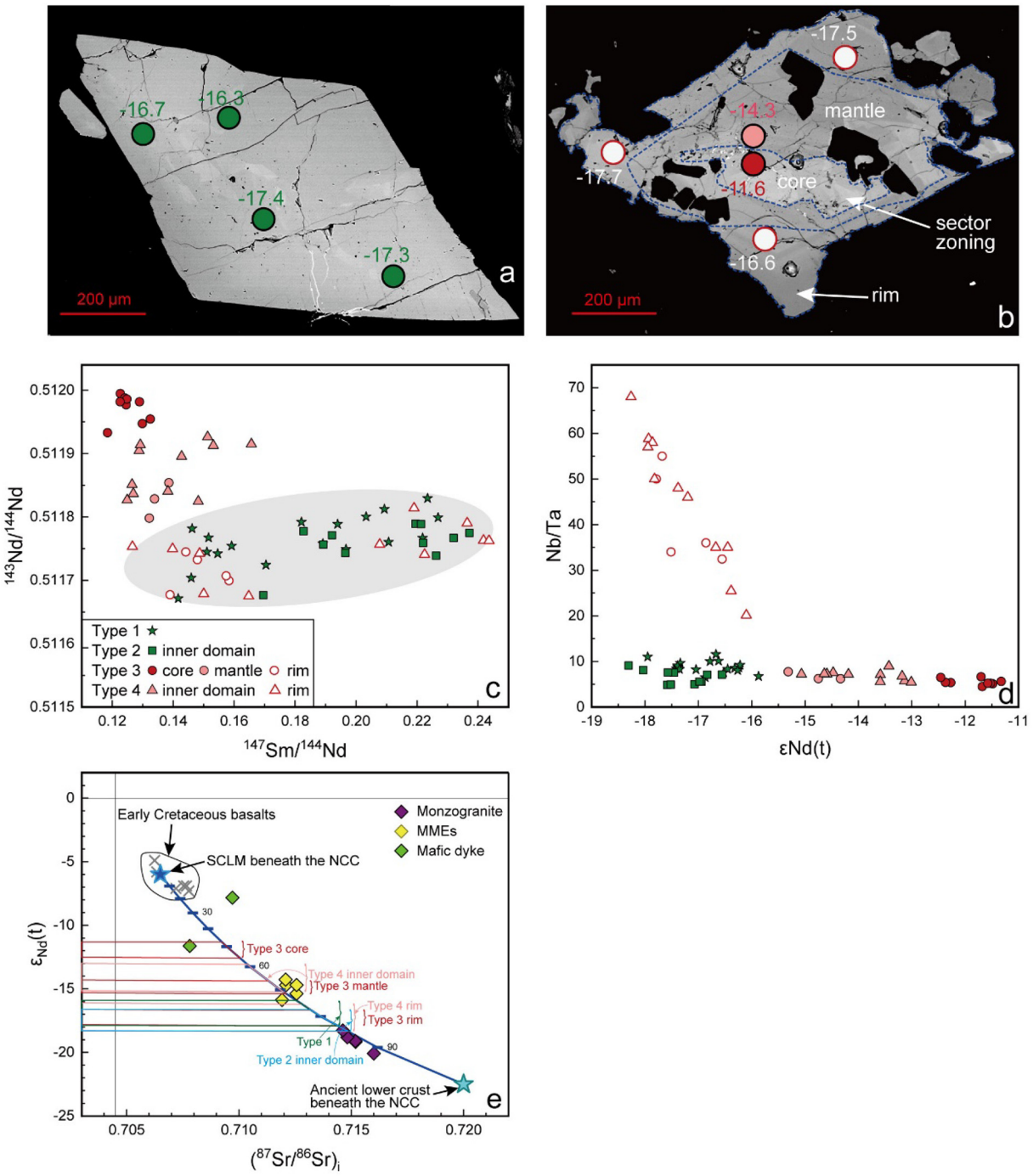

Fig. 9. Intragrain and intergrain $\varepsilon_{Nd}(t)$ variation of titanite. (a) Type 1 titanite in the monzogranite shows nearly uniform $\varepsilon_{Nd}(t)$ within the grain; (b) type 3 titanite in the MMEs shows variable $\varepsilon_{Nd}(t)$ in the core, mantle and rim; (c) plot of $^{147}Sm/^{144}Nd$ versus $^{143}Nd/^{144}Nd$ for the four types of titanite in the MMEs and host monzogranite; (d) plot of $\varepsilon_{Nd}(t)$ versus Nb/Ta for the four types of titanite in the MMEs and host monzogranite; (e) plot of $(^{87}Sr/^{86}Sr)_i$ versus $\varepsilon_{Nd}(t)$ of the MMEs and monzogranite of the Sanguliu pluton, and adjacent mafic dykes. Noted that the $\varepsilon_{Nd}(t)$ values of the four types of titanite are marked on the binary mixing line of the SCLM (subcontinental lithospheric mantle) and ancient lower crust beneath the NCC. Data sources: Early Cretaceous basalts (Zhou et al., 2001); The SCLM and ancient lower crust beneath the NCC (Yang et al., 2004). The monzogranite and the MMEs of the Sanguliu pluton and mafic dykes adjacent to the pluton (our unpublished data).

titanite (Fig. 9d), indicating that they likely crystallized from granitic magmas, rather than the mixed magmas. However, the rims of types 3 and 4 titanite have relatively high F and low Ta to that of type 1 titanite (Fig. 6b, 8a), and they show very contrasting Nb/Ta and Th/U compared to that of type 1 titanite (Fig. 8b). In general, Nb and F are more incompatible than Ta and tend to be enriched in fluids and evolved magmas (Prowatke and Klemme, 2005; Smith et al., 2009; Tiepolo et al., 2002). The dramatic increase of Nb/Ta in the rims of types 3 and 4 titanite may be attributed to the breakdown of biotite and amphibole in the late magmatic stage, which released more Nb and less Ta into the evolved melts (Chen et al., 2013; Chen and Zheng, 2015), and the solubility of Nb would increase in F-rich fluids (Smith et al., 2009). Therefore, the titanite that crystallizes from more evolved granitic magmas tend to be enriched in F and have high Nb/Ta. Uranium is also incompatible and enriched in fluid/residual melts (Williams and Gill, 1989), so low Th/U of the rims of types 3 and 4 titanite is also consistent with

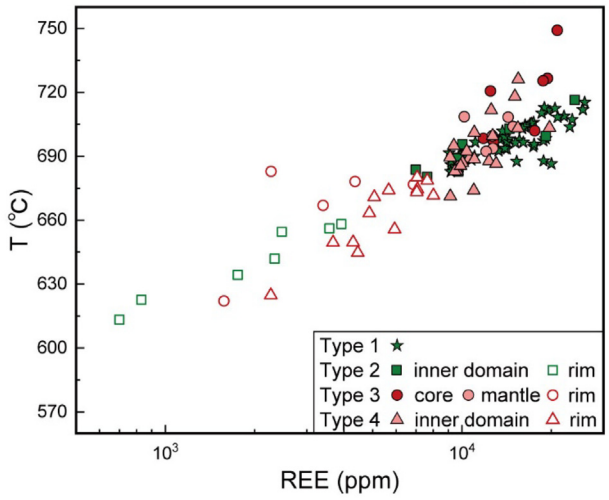

Fig. 10. Plot of REE versus calculated crystallization temperature (T) of the four types of titanite on the basis of the Zr-in-titanite thermometry which is expressed as T (°C) = (7708 + 960P)/[10.52 - log(a_{TiO_2}) - log(a_{SiO_2}) - Log(ppm Zr, titanite)] - 273. It is assumed that $a_{TiO_2} = 0.5$ and $a_{SiO_2} = 1$ according to the mineral assemblage containing quartz and zircon but without rutile, Zr is measured by LA-ICP-MS, and pressure (P) is obtained using the amphibole geobarometer (Johnson and Rutherford, 1989; Yang et al., 2017).

crystallization from hydrated, evolved, granitic magmas (e.g., Chen et al., 2013; Li et al., 2010).

The deuteric rim of type 2 titanite contains higher F, Nb/Ta and δEu than the rims of types 3 and 4 titanite against similar Th/U (Figs. 6b, 8b, c). Unlike the rim of type 3 titanite that has much higher U than that of the mantle and core (Fig. 12), the rim of type 2 titanite contains much lower U than that of the inner domain of type 2 (Fig. 11). This is probably because type 2 titanite crystallized concurrently with zircon, as zircon inclusions are enclosed within the rim (Fig. 4d) and zircon is often rich in U. Eu^{2+} can be released from plagioclase during albitization associated with low-temperature deuteric fluids (Kontonikas-Charos et al., 2019), leading to the positive Eu anomaly in the rim of type 2 (*c.f.*, Olierook et al., 2019). Therefore, the rim of type 2 titanite is likely attributed to the overgrowth of deuteric fluid under subsolidus conditions. The deuteric fluids may penetrate the inner domain of type 2 titanite along cracks (Fig. 4d). A similar case has been reported in the titanite of the Roxby Downs granite, the host of the Olympic Dam IOCG deposit (Kontonikas-Charos et al., 2019).

7.4. A three-stage growth model for the titanite in the MMEs

The core of type 3 titanite shows embayment (Fig. 4e, f), which is typical of a disequilibrium texture and can be attributed to the resorption of the core by the mantle. The assemblage of quartz ± plagioclase ± K-feldspar in the mantle of type 3 titanite displays titanite-

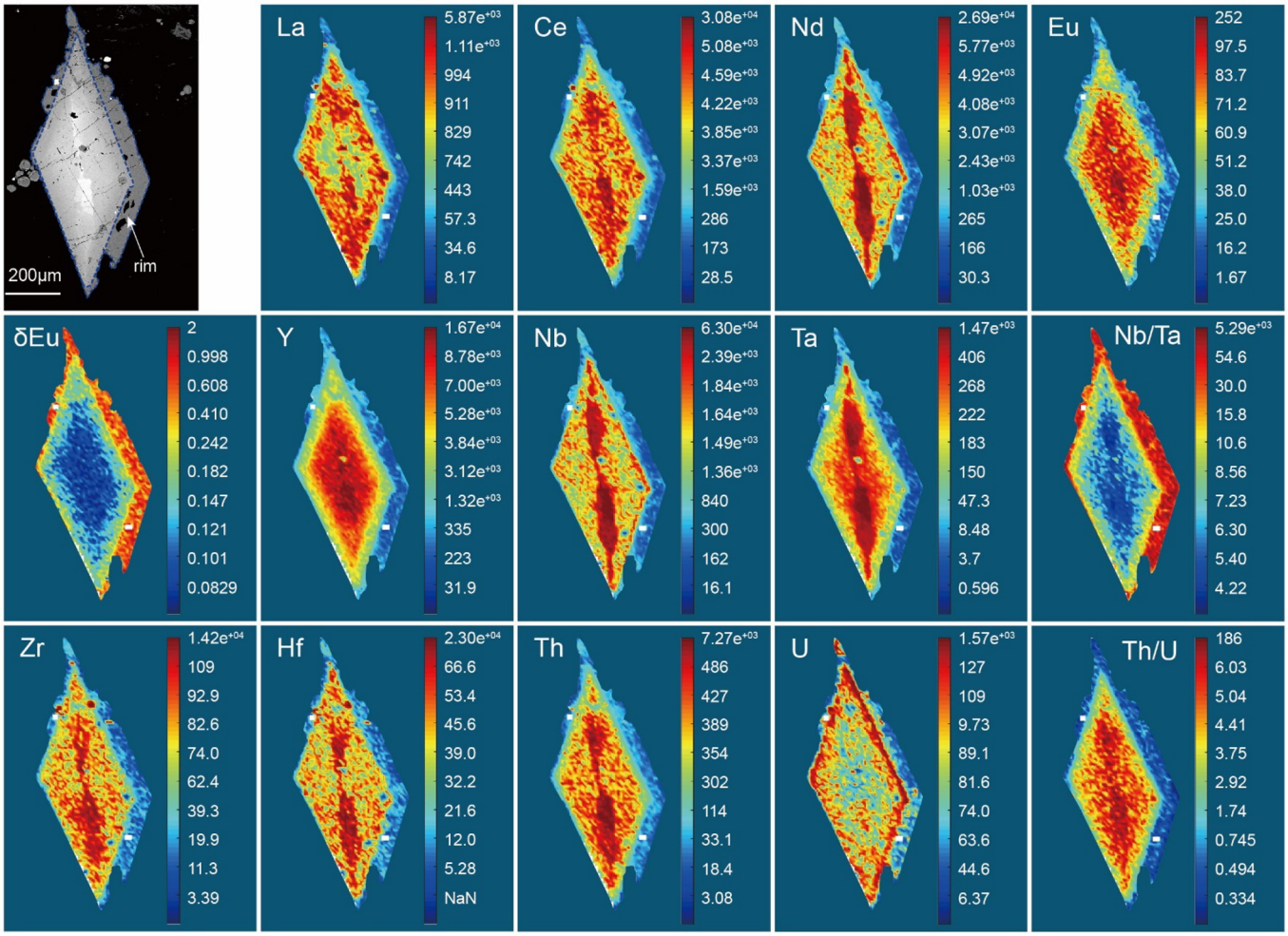

Fig. 11. The BSE image and trace element mapping for a type 2 titanite grain in the monzogranite of the Sanguliu granitic pluton showing that REE, Y, Nb, Ta, Zr, Hf, Th and Th/U gradually decreased, δEu and Nb/Ta gradually increased, and U increased first and then decreased from the inner domain to rim.

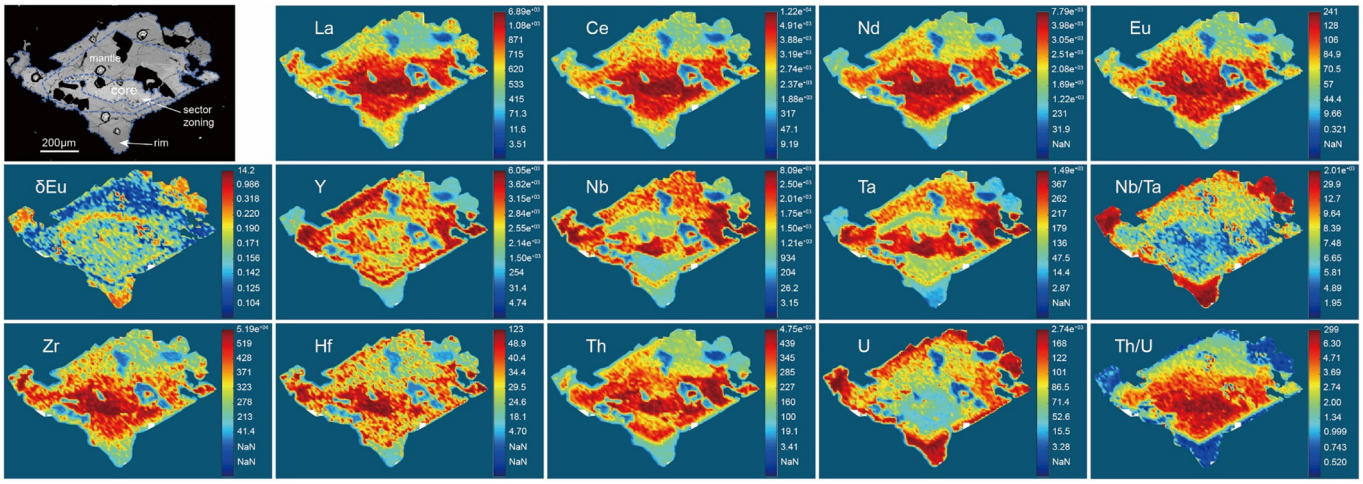

Fig. 12. The BSE image and trace element mapping for a type 3 titanite grain in the MMEs of the Sanguliu granitic pluton showing that REE, Zr, Hf, Th, Th/U gradually decreased, Nb/Ta and U gradually increased from the core to mantle and then to rim, whereas Nb, Ta and Y suddenly decreased at the dissolved boundary between the core and mantle.

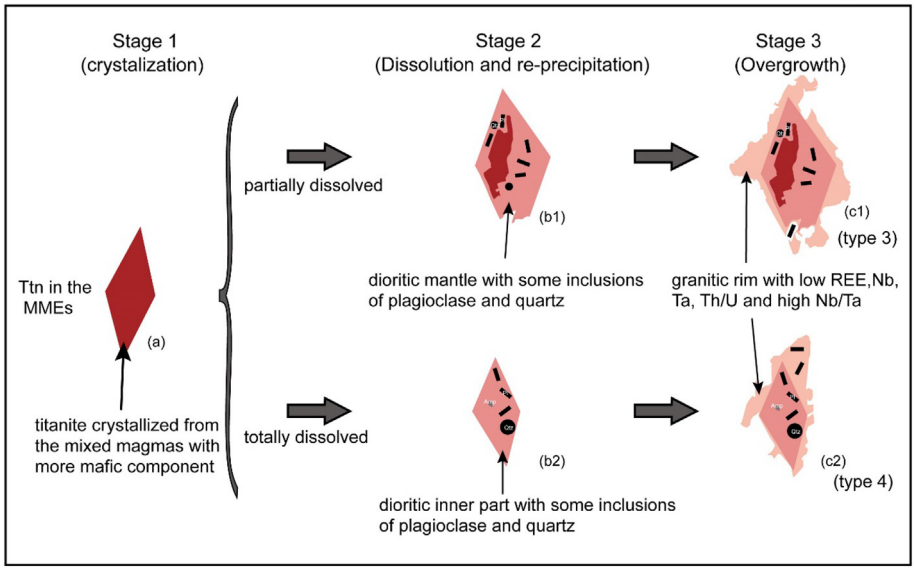

Fig. 13. A cartoon illustrating a three-stage growth model of the titanite from the MMEs in the Sanguliu granitic pluton.

plagioclase ocelli texture (Fig. 3f), which is attributed to a magma mixing process (*c.f.*, Hibbard, 1981). The rims of types 3 and 4 titanite are discontinuous and irregular and show transitional boundaries with the mantle (Fig. 4e–i). These indicate that the titanite in the MMEs of the Sanguliu granitic pluton may have experienced complex growth process. On the basis of $\varepsilon_{Nd}(t)$ and trace element mapping of type 3 titanite, we propose a three-stage growth model to explain the core-mantle-rim texture of the titanite in the MMEs. The first stage began with crystallization of titanite from mixed magmas with more mafic components, and sector and fir-tree zoning developed in the titanite (Fig. 13a). The second stage was triggered by chemical disequilibrium so that the first-stage titanite was resorbed by an ambient, dioritic melt (Fig. 13b). The first-stage titanite may have been partially or totally dissolved by the ambient melt, and only some remnants were preserved as the core of type 3. Simultaneously, re-precipitation of titanite from the ambient, dioritic melt formed the second-stage domain, appearing as the mantle of type 3 and the inner domain of type 4 titanite (Fig. 13b). The third-stage involved the overgrowth rim of the titanite from the evolved granitic magma (Fig. 13c). Therefore, the core-mantle-rim texture of the titanite in the MMEs recorded vigorous processes of magma mixing. The core and mantle of the titanite crystallized in different stages of mixed magmas, and the rim of the titanite crystallized from the evolved granitic magma (Fig. 13c). In this scenario, similar $\varepsilon_{Nd}(t)$ values of the mantle of types 3 and 4 titanite and the MMEs indicate that magma mixing may have taken place in a magma chamber at the depth, and the molten mixed magma may have been trapped in granitic magmas prior to the emplacement of the Sanguliu pluton.

8. Conclusions

Titanite grains in the MMEs and host monzogranite of the Sanguliu granitic pluton have similar U–Pb ages, coincident with the peak of the destruction of the NCC. The titanite of the MMEs displays the core-mantle-rim texture which resulted from a three-stage growth process during magma mixing in a magma chamber at depth. The core and mantle of the titanite crystallized from mixed magmas with variable proportions of two end members, whereas the rim crystallized from an evolved granitic melt. The disequilibrium textures of the titanite

were likely developed due to the dissolution and re-precipitation process when primary titanite was in chemical disequilibrium with ambient, dioritic magmas after the onset of magma mixing.

Declaration of Competing Interest

The authors declare that they have no known competing financial interests or personal relationships that could have appeared to influence the work reported in this paper.

Acknowledgement

he study was supported by the Chinese National Key Research and Development Program (2016YFC0600103) and Science and Technology Planning of Guangdong Province, China (2017B030314175/2020 B1212060055). We thank Yueheng Yang, Shitou Wu, Qian Ma and Han Zhao for the assistance during the U–Pb dating and in situ Nd isotope analyses, Fangyue Wang for the assistance of LA-ICPMS mapping, and Yisheng Zhu, Hao Wang, Jinfeng Sun for the assistance in the field work. Constructive comments from two anonymous reviewers and the editor, Xianhua Li, are appreciated. Mei-Fu Zhou kindly helped to polish the English of the revised version of the manuscript.

Appendix A. Supplementary data

Supplementary data to this article can be found online at https://doi.org/10.1016/j.lithos.2021.106138.

References

Barbarin, B., 2005. Mafic magmatic enclaves and mafic rocks associated with some granitoids of the Central Sierra Nevada batholith, California: Nature, origin, and relations with the hosts. Lithos 80, 155–177. https://doi.org/10.1016/j.lithos.2004.05.010.

Baxter, S., Feely, M., 2002. Field and petrographic evidence for magma mixing and mingling in Granitoids: examples from the Galway Granite. Connemara. Mineral. Petrol. 76, 63–74. https://doi.org/10.1007/s00710-001-0178-8.

Bruand, E., Storey, C., Fowler, M., 2014. Accessory mineral chemistry of high Ba-Sr granites from Northern Scotland: Constraints on petrogenesis and records of whole-rock Signature. J. Petrol. 55, 1619–1651. https://doi.org/10.1093/petrology/egu037.

Cao, M.J., Qin, K.Z., Li, G.M., Evans, N.J., Jin, L.Y., 2015. In situ LA-(MC)-ICP-MS trace element and Nd isotopic compositions and genesis of polygenetic titanite from the Baogutu reduced porphyry Cu deposit, Western Junggar, NW China. Ore Geol. Rev. 65, 940–954. https://doi.org/10.1016/j.oregeorev.2014.07.014.

Chen, Y.X., Zheng, Y.F., 2015. Extreme Nb/Ta fractionation in metamorphic titanite from ultrahigh-pressure metagranite. Geochim. Cosmochim. Acta 150, 53–73. https://doi.org/10.1016/j.gca.2014.12.002.

Chen, Y.X., Zheng, Y.F., Hu, Z., 2013. Polyphase growth of accessory minerals during continental collision: Geochemical evidence from ultrahigh-pressure metamorphic gneisses in the Sulu orogen. Lithos 177, 245–267. https://doi.org/10.1016/j.lithos.2013.07.010.

Cherniak, D.J., 2015. Nb and Ta diffusion in titanite. Chem. Geol. 413, 44–50. https://doi.org/10.1016/j.chemgeo.2015.08.010.

Davidson, J.P., Morgan, D.J., Charlier, B.L.A., 2007. Isotopic microsampling of magmatic rocks. Elements 3, 253–259. https://doi.org/10.2113/gselements.3.4.253.

Davis, G.A., Darby, B.J., Yadong, Z., Spell, T.L., 2002. Geometric and temporal evolution of an extensional detachment fault, Hohhot metamorphic core complex, Inner Mongolia, China. Geology 30, 1003–1006. https://doi.org/10.1130/0091-7613(2002)030<1003:GATEOA>2.0.CO;2.

Farner, M.J., Lee, C.T.A., Putirka, K.D., 2014. Mafic-felsic magma mixing limited by reactive processes: a case study of biotite-rich rinds on mafic enclaves. Earth Planet. Sci. Lett. 393, 49–59. https://doi.org/10.1016/j.epsl.2014.02.040.

Flinders, J., Clemens, J.D., 1996. Non-linear dynamics, chaos, complexity and enclaves in granitoid magmas. Spec. Pap. Geol. Soc. Am. 315, 217–223. https://doi.org/10.1130/0-8137-2315-9.217.

Frost, B.R., Chamberlain, K.R., Schumacher, J.C., 2000. Sphene (titanite): phase relations and role as a geochronometer. Chem. Geol. 172, 131–148. https://doi.org/10.1016/S0009-2541(00)00240-0.

Fu, Y., Sun, X.M., Zhou, H.Y., Lin, H., Yang, T.J., 2016. In-situ LA-ICP-MS U-Pb geochronology and trace elements analysis of polygenetic titanite from the giant Beiya gold-polymetallic deposit in Yunnan Province, Southwest China. Ore Geol. Rev. 77, 43–56. https://doi.org/10.1016/j.oregeorev.2016.02.001.

Green, T.H., Pearson, N.J., 1986. Rare-earth element partitioning between sphene and coexisting silicate liquid at high pressure and temperature. Chem. Geol. 55, 105–119. https://doi.org/10.1016/0009-2541(86)90131-2.

Griffin, W.L., 2008. GLITTER: Data reduction software for laser ablation ICP-MS. In: Sylvester, P. (Ed.), Laser Ablation-ICP-MS in the Earth Sciences: Current Practices and Outstanding Issues. Mineralogical Association of Canada Short Course. vol. 40, pp. 308–311.

Griffin, W.L., Wang, X., Jackson, S.E., Pearson, N.J., O'Reilly, S.Y., Xu, X., Zhou, X., 2002. Zircon chemistry and magma mixing, SE China: In-situ analysis of Hf isotopes, Tonglu and Pingtan igneous complexes. Lithos 61, 237–269. https://doi.org/10.1016/S0024-4937(02)00082-8.

Hibbard, M.J., 1981. The magma mixing origin of mantled feldspars. Contrib. Mineral. Petrol. 76, 158–170. https://doi.org/10.1007/BF00371956.

Higgins, J.B., Ribbe, P.H., 1976. The crystal chemistry and space groups of natural and synthetic titanites. Am. Mineral. 61, 878–888.

Hayden, L.A., Watson, E.B., Wark, D.A., 2008. A thermobarometer for sphene (titanite). Contrib. to Mineral. Petrol. 155, 529–540. https://doi.org/10.1007/s00410-007-0256-y.

Jiang, P., Yang, K.F., Fan, H.R., Liu, X., Cai, Y.C., Yang, Y.H., 2016. Titanite-scale insights into multi-stage magma mixing in Early Cretaceous of NW Jiaodong terrane, North China Craton. Lithos 258–259, 197–214. https://doi.org/10.1016/j.lithos.2016.04.028.

Johannes, W., Holtz, F., 1996. Formation of Granitic Magmas by Dehydration Melting 264–301. https://doi.org/10.1007/978-3-642-61049-3_9.

Johnson, M.C., Rutherford, M.J., 1989. Experimental calibration of the aluminum-in-hornblende geobarometer with application of Long Valley caldera (California) volcanic rocks. Geology 17, 837–841. https://doi.org/10.1130/0091-7613(1989)017<0837:ECOTAI>2.3.CO;2.

Kontonikas-Charos, A., Ehrig, K., Cook, N.J., Ciobanu, C.L., 2019. Crystal chemistry of titanite from the Roxby Downs Granite, South Australia: insights into petrogenesis, subsolidus evolution and hydrothermal alteration. Contrib. Mineral. Petrol. 174, 1–20. https://doi.org/10.1007/s00410-019-1594-2.

Lesher, C.E., 1990. Decoupling of chemical and isotopic exchange during magma mixing. Nature 344, 235–237. https://doi.org/10.1038/344235a0.

Li, J.W., Deng, X.D., Zhou, M.F., Liu, Y.S., Zhao, X.F., Guo, J.L., 2010. Laser ablation ICP-MS titanite U-Th-Pb dating of hydrothermal ore deposits: a case study of the Tonglushan Cu-Fe-au skarn deposit, SE Hubei Province, China. Chem. Geol. 270, 56–67. https://doi.org/10.1016/j.chemgeo.2009.11.005.

Lin, J.Q., Tan, D.J., Chi, X.G., Bi, L.J., Xie, C.F., Xu, W.L., 1992. Mesozoic granites in Jiao-Liao peninsula. Science Press, Beijing, p. 208 (in Chinese with English abstract).

Liu, D.Y., Nutman, A.P., Compston, W., Wu, J.S., Shen, Q.H., 1992. Remnants of ≥3800 Ma crust in the Chinese part of the Sino- Korean craton. Geology 20, 339–342. https://doi.org/10.1130/0091-7613(1992)020<0339:ROMCIT>2.3.CO;2.

Liu, J.L., Davis, G.A., Lin, Z.Y., Wu, F.Y., 2005. The Liaonan metamorphic core complex, Southeastern Liaoning Province, North China: a likely contributor to cretaceous rotation of Eastern Liaoning, Korea and contiguous areas. Tectonophysics 407, 65–80. https://doi.org/10.1016/j.tecto.2005.07.001.

Lu, S.N., Zhao, G.C., Wang, H.C., Hao, G.J., 2008. Precambrian metamorphic basement and sedimentary cover of the North China Craton: a review. Precambrian Res. 160, 77–93. https://doi.org/10.1016/j.precamres.2007.04.017.

Ludwig, K.R., 2012. User's Manual for Isoplot 4.15. 5. Berkley Geochronology Center Special Publication, p. 75.

Ma, Q., Evans, N.J., Ling, X.X., Yang, J.H., Wu, F.Y., Zhao, Z.D., Yang, Y.H., 2019. Natural Titanite Reference Materials for In Situ U-Pb and Sm-Nd Isotopic Measurements by LA-(MC)-ICP-MS. Geostand. Geoanal. Res. 43, 355–384. https://doi.org/10.1111/ggr.12264.

Mcleod, G.W., Dempster, T.J., Faithfull, J.W., 2011. Deciphering magma-mixing processes using zonedtitanite from the Ross of Mull Granite. Scotland. J. Petrol. 52, 55–82. https://doi.org/10.1093/petrology/egq071.

Nakada, R., Takahashi, Y., Tanimizu, M., 2016. Cerium stable isotope ratios in ferromanganese deposits and their potential as a paleo-redox proxy. Geochim. Cosmochim. Acta 181, 89–100. https://doi.org/10.1016/j.gca.2016.02.025.

Olierook, H.K.H., Taylor, R.J.M., Erickson, T.M., Clark, C., Reddy, S.M., Kirkland, C.L., Jahn, I., Barham, M., 2019. Unravelling complex geologic histories using U–Pb and trace element systematics of titanite. Chem. Geol. 504, 105–122. https://doi.org/10.1016/j.chemgeo.2018.11.004.

Paterson, B.A., Stephens, W.E., 1992. Kinetically induced compositional zoning in titanite: implications for accessory-phase/melt partitioning of trace elements. Contrib. Mineral. Petrol. 109, 373–385. https://doi.org/10.1007/BF00283325.

Piccoli, P., Candela, P., Rivers, M., 2000. Interpreting magmatic processes from accessory phases: Titanite–a small recorder of large-scale processes. Trans. R. Soc. Edinb. Earth Sci. 91, 257–267. https://doi.org/10.1017/s0263593300007422.

Plail, M., Edmonds, M., Woods, A.W., Barclay, J., Humphreys, M.C.S., Herd, R.A., Christopher, T., 2018. Mafic enclaves record syn-eruptive basalt intrusion and mixing. Earth Planet. Sci. Lett. 484, 30–40. https://doi.org/10.1016/j.epsl.2017.11.033.

Prowatke, S., Klemme, S., 2005. Effect of melt composition on the partitioning of trace elements between titanite and silicate melt. Geochim. Cosmochim. Acta 69, 695–709. https://doi.org/10.1016/j.gca.2004.06.037.

Shannon, R.D., 1976. Revised effective ionic radii and systematic studies of interatomic distances in halides and chalcogenides. Acta Crystallogr. Sect. A 32, 751–767. https://doi.org/10.1107/S0567739476001551.

Smith, M.P., Storey, C.D., Jeffries, T.E., Ryan, C., 2009. In situ U-Pb and trace element analysis of accessory minerals in the Kiruna District, Norrbotten, Sweden: New constraints on the timing and origin of mineralization. J. Petrol. 50, 2063–2094. https://doi.org/10.1093/petrology/egp069.

Sun, J.F., Yang, J.H., Wu, F.Y., Li, X.H., Yang, Y.H., Xie, L.W., Wilde, S.A., 2010. Magma mixing controlling the origin of the Early Cretaceous Fangshan granitic pluton, North China Craton: In situ U-Pb age and Sr-, Nd-, Hf- and O-isotope evidence. Lithos 120, 421–438. https://doi.org/10.1016/j.lithos.2010.09.002.

Sun, S.S., McDonough, W.F., 1989. Chemical and isotopic systematics of oceanic basalts: Implications for mantle composition and processes. Geol. Soc. Spec. Publ. 42, 313–345 doi:10.1144/GSL.SP.1989.042.01.19.

Sun, J.F., Yang, J.H., Wu, F.Y., Xie, L.W., Yang, Y.H., Liu, Z.C., Li, X.H., 2012. In situ U-Pb dating of titanite by LA-ICPMS. Chin. Sci. Bull. 57, 2506–2516. https://doi.org/10.1007/s11434-012-5177-0.

Tera, F., Wasserburg, G.J., 1972. U-Th-Pb systematics in three Apollo 14 basalts and the problem of initial Pb in lunar rocks. Earth Planet. Sci. Lett. 14, 281–304. https://doi.org/10.1016/0012-821X(72)90128-8.

Tiepolo, M., Oberti, R., Vannucci, R., 2002. Trace-element incorporation in titanite: Constraints from experimentally determined solid/liquid partition coefficients. Chem. Geol. 191, 105–119. https://doi.org/10.1016/S0009-2541(02)00151-1.

Ventura, G., Del Gaudio, P., Iezzi, G., 2006. Enclaves provide new insights on the dynamics of magma mingling: a case study from Salina Island (Southern Tyrrhenian Sea, Italy). Earth Planet. Sci. Lett. 243, 128–140. https://doi.org/10.1016/j.epsl.2006.01.004.

Vernon, R.H., 1984. Microgranitoid enclaves in granites - Globules of hybrid magma quenched in a plutonic environment. Nature 309, 438–439. https://doi.org/10.1038/309438a0.

Wan, Y.S., Liu, D.Y., Wang, S.J., Dong, C.Y., Yang, E.X., Wang, W., Zhou, H.Y., Ning, Z.G., Du, L.L., Yin, X.Y., Xie, H.Q., Ma, M.Z., 2010. Juvenile magmatism and crustal recycling at the end of the Neoarchean in western Shandong Province, North China Craton: evidence from SHRIMP zircon dating. Am. J. Sci. 310, 1503–1552. https://doi.org/10.2475/10.2010.11.

Wan, Y.S., Liu, D.Y., Wang, S.J., Yang, E.X., Wang, W., Dong, C.Y., Zhou, H.Y., Du, L.L., Yang, Y.H., Diwu, C., 2011. ~2.7Ga juvenile crust formation in the North China Craton (Taishan-Xintai area, western Shandong Province): further evidence of an understated event from U-Pb dating and Hf isotopic composition of zircon. Precambrian Res. 186, 169–180. https://doi.org/10.1016/j.precamres.2011.01.015.

Wang, F.Y., Ge, G., Ning, S.Y., Nie, L.Q., Zhong, G.X., White, N.C., 2017. A new approach to LA-ICP-MS mapping and application in geology. Acta Petrol. Sin. 33, 3422–3436 (in Chinese with English abstract).

Watson, E.B., Yan Liang, 1995. A simple model for sector zoning in slowly grown crystals: implications for growth rate and lattice diffusion, with emphasis on accessory minerals in crustal rocks. Am. Mineral. 80, 1179–1187. https://doi.org/10.2138/am-1995-11-1209.

Wei, J.H., Liu, C.Q., Li, Z.D., Zhao, Y.X., 2003. U-Pb, Rb-Sr isotopic dating of the diagenesis and mineralization of gold deposit in the Dandong area. Acta Geol. Sin. 77, 113–119 (in Chinese with English abstract).

Williams, R.W., Gill, J.B., 1989. Effects of partial melting on the uranium decay series. Geochim. Cosmochim. Acta 53, 1607–1619. https://doi.org/10.1016/0016-7037(89)90242-1.

Wones, D.R., 1989. Significance of the assemblage titanite + magnetite + quartz in granitic rocks. Am. Mineral. 74, 744–749.

Wu, F.Y., Lin, J.Q., Wilde, S.A., Zhang, X., Yang, J.H., 2005a. Nature and significance of the early cretaceous giant igneous event in eastern China. Earth Planet. Sci. Lett. 233, 103–119. https://doi.org/10.1016/j.epsl.2005.02.019.

Wu, F.Y., Yang, J.H., Wilde, S.A., Zhang, X.O., 2005b. Geochronology, petrogenesis and tectonic implications of Jurassic granites in the Liaodong Peninsula, NE China. Chem. Geol. 221, 127–156. https://doi.org/10.1016/j.chemgeo.2005.04.010.

Wu, F.Y., Yang, Y.H., Mitchell, R.H., Li, Q.L., Yang, J.H., Zhang, Y. Bin, 2010. In situ U-Pb age determination and Nd isotopic analysis of perovskites from kimberlites in southern Africa and Somerset Island, Canada. Lithos 115, 205–222. https://doi.org/10.1016/j.lithos.2009.12.010.

Wu, F.Y., Yang, J.H., Xu, Y.G., Wilde, S.A., Walker, R.J., 2019. Destruction of the North China craton in the mesozoic. Annu. Rev. Earth Planet. Sci. 47, 173–195. https://doi.org/10.1146/annurev-earth-053018-060342.

Yang, J.H., Zhou, X.H., 2002. Rb-Sr, Sm-Nd, and Pb isotopes systematics of pyrite: Implications for the age and genesis of lode gold deposits. Geology 29, 711–714. https://doi.org/10.1130/0091-7613(2001)029<0711:RSSNAP>2.0.CO;2.

Yang, J.H., Wu, F.Y., Chung, S.L., Wilde, S.A., Chu, M.F., 2004. Multiple sources for the origin of granites: Geochemical and Nd/Sr isotopic evidence from the Gudaoling granite and its mafic enclaves, Northeast China. Geochim. Cosmochim. Acta 68, 4469–4483. https://doi.org/10.1016/j.gca.2004.04.015.

Yang, J.H., Wu, F.Y., Chung, S.L., Wilde, S.A., Chu, M.F., 2006. A hybrid origin for the Qianshan A-type granite, Northeast China: Geochemical and Sr-Nd-Hf isotopic evidence. Lithos 89, 89–106. https://doi.org/10.1016/j.lithos.2005.10.002.

Yang, J.H., Wu, F.Y., Wilde, S.A., Xie, L.W., Yang, Y.H., Liu, X.M., 2007. Tracing magma mixing in granite genesis: in situ U - Pb dating and Hf-isotope analysis of zircons. Contrib. Mineral. Petrol. 153, 177–190. https://doi.org/10.1007/s00410-006-0139-7.

Yang, Y.H., Sun, J.F., Xie, L.W., Fan, H.R., Wu, F.Y., 2008. In situ Nd isotopic measurement of natural geological materials by LA-MC-ICPMS. Chin. Sci. Bull. 53, 1062–1070. https://doi.org/10.1007/s11434-008-0166-z.

Yang, Y., Wang, X.X., Yu, X.W., Ke, C.H., Wang, L.G., Guo, R.P., Wang, S.A., Li, X.X., 2017. Chemical composition of biotite and amphibole from Mesozoic granites in northwestern Jiaodong Peninsula, China, and their implications. Acta Petrol. Sin. 33, 3123–3136 (in Chinese with English abstract).

Zhou, X.H., Zhang, G.H., Yang, J.H., Chen, W.J., Sun, M., 2001. Sr–Nd–Pb isotope mapping of late Mesozoic volcanic rocks across northern margin of North China Craton and implications to geodynamics processes. Geochem 30, 10–23 (in Chinese with English abstract).